symmetry

MDPI

Article

Under Sulfate Dry–Wet Cycling: Exploring the Symmetry of the Mechanical Performance Trend and Grey Prediction of Lightweight Aggregate Concrete with Silica Powder Content

Hailong Wang *, Yaolu Chen and Hongshan Wang

College of Water Conservancy and Civil Engineering, Inner Mongolia Agricultural University, Hohhot 010018, China; cyl991102@163.com (Y.C.); fch001215@163.com (H.W.)
* Correspondence: nndwhl@imau.edu.cn

Abstract: In order to improve the mechanical properties and durability of lightweight aggregate concrete in extreme environments, this study utilized Inner Mongolia pumice as the coarse aggregate to formulate pumice lightweight aggregate concrete (P-LWAC) with a silica powder content of 0%, 2%, 4%, 6%, 8%, and 10%. Under sulfate dry–wet cycling conditions, this study mainly conducted a mass loss rate test, compressive strength test, NMR test, and SEM test to investigate the improvement effect of silica powder content on the corrosion resistance performance of P-LWAC. In addition, using grey prediction theory, the relationship between pore characteristic parameters and compressive strength was elucidated, and a grey prediction model GM (1,3) was established to predict the compressive strength of P-LWAC after cycling. Research indicates that under sulfate corrosion conditions, as the cycle times and silica powder content increased, the corrosion resistance of P-LWAC showed a trend of first increasing and then decreasing. At 60 cycles, P-LWAC with a content of 6% exhibited the lowest mass loss rate and the highest relative dynamic elastic modulus, compressive strength, and corrosion resistance coefficient. From the perspective of data distribution, various durability indicators showed a clear mirror symmetry towards both sides with a silica powder content of 6% as the symmetrical center. The addition of silica fume reduced the porosity and permeability of P-LWAC, enhanced the saturation degree of bound fluid, and facilitated internal structural development from harmful pores towards less harmful and harmless pores, a feature most prominent at the 6% silica fume mixing ratio. In addition, a bound fluid saturation and pore size of 0.02~0.05 μm/% exerted the most significant influence on the compressive strength of P-LWAC subjected to 90 dry–wet cycles. Based on these two factors, grey prediction model GM (1,3) was established. This model can accurately evaluate the durability of P-LWAC, improving the efficiency of curing decision-making and construction of concrete materials.

Keywords: pumice lightweight aggregate concrete; dry–wet cycle; sulfate; pore structure; grey model (1,3)

Citation: Wang, H.; Chen, Y.; Wang, H. Under Sulfate Dry–Wet Cycling: Exploring the Symmetry of the Mechanical Performance Trend and Grey Prediction of Lightweight Aggregate Concrete with Silica Powder Content. *Symmetry* **2024**, *16*, 275. https://doi.org/10.3390/sym16030275

Academic Editor: Tomasz Lewiński

Received: 17 January 2024
Revised: 16 February 2024
Accepted: 22 February 2024
Published: 26 February 2024

1. Introduction

Thus far, lightweight aggregate concrete (LWAC) has played a crucial role in practical applications. Compared with ordinary concrete, LWAC is lightweight, has high strength, possesses strong corrosion resistance, and is economically and practically viable as a concrete material [1–3]. Due to its distinctive characteristics, it has become one of the most important materials in contemporary civil engineering, widely used in roads, buildings, bridges, dams, water conservancy projects, and other fields. Lightweight aggregates can be categorized based on their source into natural pumice, artificial clay, and industrial waste residue. Natural pumice offers advantages such as high strength, acid and alkali resistance, and corrosion resistance and is free of pollution and radioactivity, making it an ideal environmentally friendly product. In Inner Mongolia, pumice possesses the advantages of a wide distribution, excellent quality, and abundant resources, thus making lightweight aggregate pumice concrete (P-LWAC) one of the preferred concrete materials

in the region. Although P-LWAC possesses good mechanical properties as a typical porous material, it is susceptible to external sulfate erosion, which disrupts the equilibrium state of pore solutions and leads to degradation. The higher soil salinity in Inner Mongolia makes this destruction more common [4–7]. Furthermore, the climate in Inner Mongolia is predominantly characterized by a temperate continental monsoon climate featuring frequent cold waves, concentrated precipitation, and alternating dry and wet conditions, all of which can accelerate the degradation of concrete structures [8–11]. Consequently, given the detrimental effects of harsh environmental conditions on P-LWAC, enhancing its durability has emerged as a critical issue.

Recently, several researchers have endeavored to enhance the mechanical properties of conventional concrete by incorporating various mixtures. Xiaosa et al., developed high-performance concrete by incorporating waste eggshell particles and waste glass powder as partial substitutes. They assessed the changes in compressive and splitting strength to ascertain the optimal substitution rate of the admixture, which was found to be 20% [12]. Zhe et al., discovered that the synergistic effect of an alkali-resistant glass fiber and expansion agent could improve the dynamic compression performance of seawater sand concrete by 12.6%. Through the introduction of the fineness modulus of residue and observation of the specimen's damage mode, they confirmed the benign synergistic effect of these components on the dynamic compressive strength of concrete [13]. Yimmy et al., employed concrete waste as recycled coarse aggregate and masonry residues as supplementary cementing material to create self-compacting concrete. They assessed its compressive performance under sulfate corrosion, discovering that the mixture demonstrated lower linear expansion and compressive strength loss compared to the reference mixture without these components [14]. Qusay et al., endeavored to incorporate wood waste as a substitute for fine aggregates in concrete. Through SEM and FTIR analysis, they discovered that a specific mix incorporating wood waste increased the concrete mixture's absorbency by 300% but reduced its compressive strength by 65.5% [15]. Verma et al., utilized recycled concrete aggregates, limestone, and metakaolin as alternative materials in the bonding system. They tested the concrete's durability by conducting slump tests, density tests, compressive strength tests, and sulfate attack tests on each mixture. The results indicated that a mix ratio of 20% kaolin and 10% limestone powder increased the compressive strength [16]. Reza et al., conducted load compression and radiation experiments on conventional concrete mixed with phosphate iron aggregate and steel powder. The results demonstrated that the highest compressive strength was obtained at a concrete age of 28 days by the specimen made with 100% ferrophosphorus, 20% steel powder, and 5% nano silica [17]. Consequently, the application of concrete is no longer confined to a single type. Incorporating various mixtures improves concrete's performance, extends its service life, and enhances its economic benefits.

Furthermore, silica powder, being a prevalent concrete additive, is noted for its strong density, freeze resistance, and corrosion resistance, making it a widely researched material [18–23]. Safdar et al., investigated the effect of micro silica powder on the tensile and bending properties of micro carbon fiber reinforced concrete. Their findings revealed that micro silica powder enhanced the binding strength and efficiency of carbon fiber microfilaments [24]. Abu et al., examined the impact of steel fiber and silica powder on the practical properties of ultra-high-performance geopolymer concrete. When the micro silica volume exceeded 15%, enhanced bonding properties between the matrix and steel fiber were noted, leading to an improvement in the mechanical and fracture characteristics of concrete. The quantity of steel fiber can be reduced by augmenting the silica powder content without altering the strength properties of the concrete [25]. Masoud utilized a dual precoating of resin and silica powder on the surface to enhance the material performance of waste tire concrete. The concrete's compressive strength, modulus of elasticity, and flexural strength are improved by these methods up to 60%, 28%, and 30%, respectively [26]. Suda et al., investigated the effects of micro silica powder and slag powder on the strength characteristics of concrete. They discovered that concrete mixed with both silica powder

and ground blast furnace slag exhibited superior mechanical properties compared to those with ground blast furnace slag alone [27]. Ali et al., employed nano silica powder as a concrete admixture to explore the compressive and tensile strength, permeability, initial setting time, wear rate, and viscosity of concrete. The findings indicated that at an optimal nano silica powder dosage of 11%, there was a 45% increase in compressive strength and an 11.5% increase in tensile strength [28].

As mentioned above, many researchers have limited their studies on the incorporation of mixtures and silica powder to idealized conditions. However, in practical engineering applications, the strength properties and durability of concrete are influenced by environmental conditions, such as dry–wet cycles, freeze–thaw cycles, and corrosion damage. Research on the enhancement of concrete's resistance to cyclic actions through the addition of silica powder is relatively scarce. Salt lakes, which are extensively distributed in Western China, possess a high salt content. The concentration of sulfate ions in these salt lakes is approximately 5–10 times higher than that in seawater. Notably, the Inner Mongolia Autonomous Region stands out as one of the areas with the highest salt content, measuring 278.96 g/L. Therefore, concrete materials in Western China are highly susceptible to sulfate attacks, especially in Inner Mongolia. The sulfate ions from the salt lakes can infiltrate the concrete through groundwater, rainfall, and natural seepage, subsequently triggering a series of deterioration reactions that impact the concrete's service life [29–32]. Simultaneously, the concrete endures damage from rainfall, evaporation, water level fluctuations, and other factors, placing it in a detrimental cycle of dryness and wetness, as well as sulfate corrosion [33–35]. Therefore, it is imperative to study the mechanical properties of concrete under the combined conditions of dry–wet cycling and sulfate corrosion [30,33,36,37].

Compressive strength is a critical indicator of the material performance of concrete, and the accurate prediction of this strength is vital for understanding its structural performance and longevity. The grey model is a method utilized for analyzing and predicting systems characterized by uncertain information, and it can accurately predict target performance based on a small amount of critical information. It holds significant practical value in predicting and preventing concrete damage [38,39]. Yongli et al., established a prediction model for the flexural tensile strength and compressive strength of concrete based on pore characteristic parameters that can accurately predict the mechanical properties of concrete [40]. Shuyun et al., created a grey prediction model for the compressive strength of self-compacting concrete rooted in pore structure parameters. This model achieved precise predictions of the strength properties of shale ceramsite concrete and facilitated the use of mechanical sand and shale ceramsite in self-compacting concrete [41]. Liu et al., established grey model GM (1,4) for predicting the compressive strength of the concrete based on the fractal dimensions of the aeolian sand lightweight aggregate concrete with pore radii of 0–0.1 μm, >0.1–10 μm and >10 μm was established in the current study [42]. Yin et al., established Grey prediction model GM (1,1) to forecast the annual production of waste concrete, thereby effectively promoting the utilization rate of waste concrete in Chongqing [43]. Bo et al., constructed a novel-structured, multivariable grey prediction model of various orders for predicting the bending strength of concrete. The model holds great significance for maintaining health and extending the service life of concrete structures [44].

To enhance the corrosion resistance of P-LWAC in extreme environments, this study investigated the changes in the mechanical properties of P-LWAC with varying silica powder contents under the combined influences of sulfate corrosion and dry–wet cycles. Furthermore, this study employed grey theory to establish a GM (1,3) prediction model for predicting the compressive strength of P-LWAC after undergoing cyclic failure. The research results of this study provide the optimal silica powder content for P-LWAC, which provides an important theoretical basis for the research and engineering design of concrete building materials, especially considering the universality and severity of salt corrosion environments on a global scale. The establishment of grey prediction models provides convenience for the durability evaluation of concrete materials and the implementation of maintenance tasks.

2. Material and Methods

2.1. Test Material

Cement: Jidong P·O 42.5 Ordinary Portland Cement, with its performance indices detailed in Table 1 and chemical component in Table 2. Coarse Aggregate: Pumice light aggregate from Hohhot, featuring an accumulation density of 706 kg·m^{-3}, apparent density of 1569 kg·m^{-3}, and water absorption rate of 12.2%. Fly Ash: Class fly ash from the Hohhot Jinqiao Power Plant. The main chemical components are shown in Table 2. Fine Aggregate: Hohhot natural river sand, medium grade, with good particle grading. The main physical properties are detailed in Table 3. Silica Powder: White powder, primarily comprising silica, calcium oxide, magnesium oxide, and sodium oxide, among others. The main chemical component is shown in Table 4. Superplasticizer: Naphthalene-based superplasticizer, a dark brown powder, water-soluble, with a 1% mass fraction, achieving a water reduction rate of 20%. Sulfate: Anhydrous sodium sulfate, analytical grade. Na_2SO_4 content $\geq$ 99.0%. Water: Ordinary tap water. The raw materials were prepared as shown in Figure 1.

Table 1. Performance indices of Jidong P·O 42. 5 ordinary Portland cement.

Fineness/%	Initial Setting Time/min	Final Setting Time/min	Stability	SO_2/%	Loss on Ignition/%	Compressive Strength/MPa		Rupture Strength/MPa	
						3 d	28 d	3 d	28 d
1.2	135	175	Qualification	22.12	1.02	26.6	54.8	5.2	8.3

Table 2. Chemical components of cement.

Element/%	SiO_2	Al_2O_3	Fe_2O_3	MgO	CaO	Other
Cement	21.29	5.20	4.11	0.49	69.50	5.41
Fly Ash	58.27	24.35	5.43	0.76	6.11	5.08

Table 3. Physical properties of river sand.

Index	Fineness Modulus	Bulk Density/ (kg·m^{-3})	Apparent Density/ (kg·m^{-3})	Mud Content/%
River sand	2.5	1465	2650	2.0

Table 4. Chemical components of silica powder.

Element	SiO_2	CaO	MgO	Na_2O	K_2O	Other
Mass fraction/%	53	22	12	0.06	0.05	12.89

Figure 1. Specimen preparation process.

2.2. Concrete Design

In the experiments, P-LWAC without silica powder served as the control group, with a water:cement ratio of 0.32. Silica powder was utilized to replace cement through an equal mass replacement method. The replacement rates of silica powder were 0%, 2%, 4%, 6%, 8%, and 10% when preparing the P-LWAC. The mix ratio followed the Design Specification for Mix Proportion of Ordinary Concrete (JGJ55-2011) [45]. The mix ratios and quantities of each group are detailed in Table 5. Preparation and curing were conducted in accordance with the Standard for Test Methods of General Concrete (GB/T50081-2002) [46] and the Technical Specification for Light Aggregate Concrete (JGJ 51-2002) [47]. The specimens were placed in a curing box for 28 days of standard maintenance, starting 24 h after pouring.

Table 5. Mix proportions of P-LWAC.

Groups	Cement/ ($kg \cdot m^{-3}$)	Sand/ ($kg \cdot m^{-3}$)	Pumice/ ($kg \cdot m^{-3}$)	Fly Ash/ ($kg \cdot m^{-3}$)	Water/ ($kg \cdot m^{-3}$)	Water Reducing Agent/($kg \cdot m^{-3}$)	Silica Powder/ ($kg \cdot m^{-3}$)	Slump/ mm
C-0	380	690	634	70	140	4.5	0	177
C-2	372.4	690	634	70	140	4.5	7.6	175
C-4	364.8	690	634	70	140	4.5	15.2	160
C-6	357.2	690	634	70	140	4.5	22.8	165
C-8	349.6	690	634	70	140	4.5	30.4	169
C-10	342	690	634	70	140	4.5	38	170

2.3. Experimental Method

2.3.1. Dry–Wet Cycle Test

In order to simulate the real erosion environment, in this study, the durability of P-LWAC was assessed using a Sulfate Dry–Wet Cycling Machine (LSY-18, Yixuan, Cangzhou, China). Referencing the Test Method Standard for Long-term Performance and Durability of Ordinary Concrete (GB/T 50082-2009) [48], the test specimen size was set at 100 mm × 100 mm × 100 mm. The corrosion solution used was a 5% Na_2SO_4 solution. The dry–wet cycle system involved soaking the sample in the solution for 16 h, air drying for 1 h, drying at a temperature of 75–85 °C for 6 h, cooling for 1 h, and completing one dry–wet cycle over 24 h, with the total number of dry–wet cycles set at 90.

During the experiment, at 0, 15, 30, 45, 60, 75, and 90 dry–wet cycles, electronic scales and a DT-20 dynamic modulus tester were used to measure the mass and lateral fundamental frequency of concrete. The measured value was the average of the test results of three samples [49,50]. The rate of mass loss served as an indicator, quantifying the deterioration in concrete quality due to factors such as environmental influences, loading conditions, and chemical interactions. The formula for this calculation is as follows (1) [51,52]. The relative dynamic modulus of elasticity is a key metric for assessing changes in the elastic characteristics of concrete when subjected to cyclic or dynamic loading. These parameters are crucial in evaluating the durability and structural integrity of concrete [53,54]. The calculation formula is as follows (2).

$$\Delta W_n = \frac{W_{0-}W_n}{W_0} \times 100\% \quad (1)$$

where ΔW_n—Mass loss rate after n dry–wet cycles (%); the result is accurate to 0.01;

W_0—LWAC mass before dry–wet cycle(g); W_n—LWAC mass after n dry–wet cycles (g).

$$P = \frac{f_n^2}{f_0^2} \times 100\% \quad (2)$$

where P—Relative dynamic elastic modulus of elasticity after n dry–wet cycles (%); the result is accurate to 0.1;

f_0—Before the dry–wet cycle test, the initial value of the lateral fundamental frequency of LWAC (Hz);

f_n—After n dry–wet cycles, LWAC lateral fundamental frequency (Hz).

2.3.2. Compressive Strength Test

In order to evaluate the mechanical properties of concrete materials. In this study, the compressive strength testing instrument for P-LWAC adopted a pressure testing instrument controlled by a microcomputer (WHY-3000, Hualong, Shanghai, China). The test specifications were carried out in accordance with the Standard Test Methods for Ordinary Concrete (GB/T 50081-2002) [46]. The sample size was 100 mm × 100 mm × 100 mm. According to the sample size, the conversion coefficient selected was 0.95. After every 15 dry–wet cycles, a compressive strength test was conducted, and the measured value was the average of the test results of three samples. The sulfate corrosion resistance of P-LWAC was represented by the corrosion resistance coefficient. This coefficient indicates the capacity of P-LWAC to preserve its structural integrity under GB/T 50081-2002 specific environmental conditions [46]. The corrosion resistance coefficient was calculated as shown in formula (3).

$$K = \frac{R_n}{R_0} \tag{3}$$

where K—corrosion resistance coefficient;

R_n—Compressive strength of the specimen after dry–wet cycle, MPa;

R_0—Compressive strength of the specimen before dry–wet circulation, MPa.

When the corrosion resistance coefficient $K \leq 0.75$, the corrosion resistance of LWAC was insufficient and damaged by sulfate corrosion [55].

2.3.3. NMR Test

In order to explore the pore structure characteristics inside concrete, this study used a NMR analyzer (MesoMR23-60, Niumag, Suzhou, China) to analyze concrete samples that had undergone 0 and 90 dry–wet cycles. Prior to measurement, concrete samples subjected to 0 and 90 dry–wet cycles were extracted using a concrete core drill and then treated with vacuum water saturation for 24 h using a vacuum saturation device (E-1010, Hitachi, Tokyo, Japan). In accordance with NMR principles, NMR data were collected using the CPMG pulse sequence [56–59]. For porous materials, the relationship between surface relaxation and pore structure is given by Formula (4) [60].

$$\frac{1}{T_2} = \rho_2 \left(\frac{S}{V}\right)_p \tag{4}$$

where T_2—Lateral relaxation times of the pore fluid, ms;

ρ_2—Lateral surface relaxation strength, μm/s;

S/V—Ratio of the pore surface area to the fluid volume, μm^{-1};

S—superficial area; p-pore;

p—the value is related to the type of specimen.

The surface relaxation strength of concrete is generally 3~10 μm/s, empirically, taking ρ_2 as 5 μm/s [61].

2.3.4. SEM Test

In this study, P-LWAC underwent micro-morphological analysis using a scanning electron microscope (S-4800, Hitachi, Tokyo, Japan). To prevent further hydration, the samples were sealed and stored in anhydrous ethanol. Prior to analysis, the samples were subjected to vacuuming and gold-sputtering. The testing apparatus utilized in this study is illustrated in Figure 2.

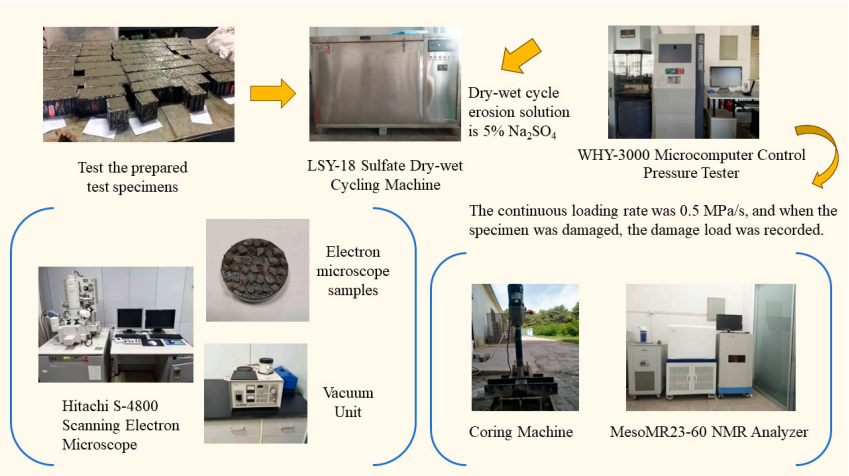

Figure 2. The testing apparatus.

3. Results and Discussion

3.1. Analysis of Mass Loss Rate

The variation in mass loss rate with the number of dry–wet cycles reflects the surface damage status of P-LWAC from a macro level. A high mass loss rate indicates that the concrete has weak resistance to environmental factors [62]. The mass loss rate under the sulfate dry–wet cycle is shown in Figure 3. Figure 3a depicts the mass loss rate of six groups of specimen samples as the number of cycles increases. Figure 3b illustrates the mass loss rate over six cycles as the silica powder content increases.

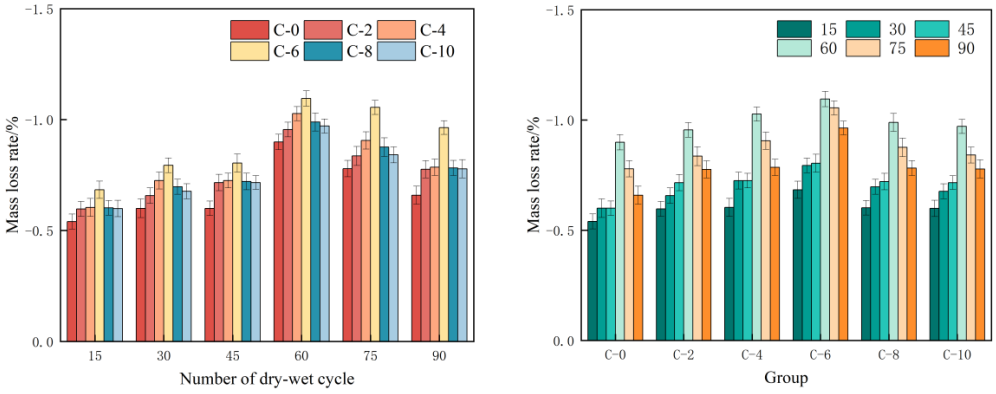

(**a**) (**b**)

Figure 3. Mass loss rate of P-LWAC. (**a**) based on number of dry-wet cycle; (**b**) based on number of silica powder content.

During the dry–wet cycle, the mass loss rate was less than zero. This phenomenon occurs because, during the salt corrosion dry–wet cycle, the concrete initially absorbs saline water; as the water evaporates, salt accumulates and crystallizes within the concrete's pores. This accumulation and subsequent crystallization of salt may initially enhance the concrete's mass, yielding a negative mass loss rate. Furthermore, the erosive process generates corrosion products within the concrete, thereby further augmenting its overall mass [63].

As shown in Figure 3a, with the increase in the number of dry–wet cycles, the overall quality loss rate of the six sample groups showed a symmetrical trend of initially increasing and then decreasing. At 60 cycles, the total mass loss rate was −5.936%, indicating that the total mass of the six groups of concrete specimens increased by 5.936% compared to the state before the dry–wet cycle. Prior to this turning point, the mass loss rate consistently decreased, signifying a continual enhancement in P-LWAC mass. Following the inflection

point, the curve exhibited an upward trend, indicative of a decline in mass. The underlying reason is that, before the 60 dry–wet cycles, SO_4^{2-} ions repeatedly penetrate and exit the concrete structure, reacting with cement hydration products to form corrosion compounds such as ettringite, which accumulate within P-LWAC, thus enhancing its mass [64,65]. After 60 dry–wet cycles, P-LWAC corrosion intensified, accompanied by surface detachment phenomena, culminating in a gradual decrease in P-LWAC mass.

As depicted in Figure 3b, during the dry–wet cycle, the mass loss rate showed a symmetrical trend of initially increasing and then decreasing. with the increase in silica powder content. When the silica powder content reached 6% at 60 cycles, the minimum mass loss rate observed was −1.095%. This is because a small or appropriate amount of silica powder can react with alkali metals in concrete, forming a more stable silicate structure, thereby enhancing concrete durability and progressively reducing the mass loss. However, excessive silica fumes disrupt the normal hydration process of cement, consequently weakening the strength and integrity of the concrete structure and relatively increasing the mass loss. When the silica powder content was 6%, an optimal amount filled the concrete's micropores, enhanced internal density, and increased the residual salt content and corrosion products, thereby improving overall concrete mass and exhibiting superior durability.

3.2. Analysis of the Relative Dynamic Elastic Modulus

The relative dynamic elastic modulus is an important indicator for evaluating the ability of concrete to maintain its elastic properties under long-term loading. A high relative dynamic elastic modulus means good durability [66]. The relative dynamic elastic modulus of P-LWAC under the sulfate dry–wet cycle is shown in Figure 4. Figure 4a shows the relative dynamic elasticity modulus of the six groups of samples as the number of cycles increases. Figure 4b shows the relative dynamic elasticity modulus under six cycles as the silica powder content increases.

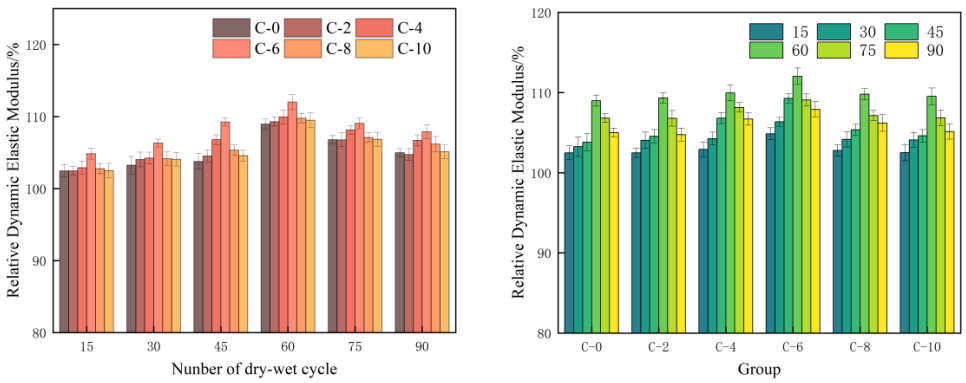

(**a**) (**b**)

Figure 4. Relative dynamic elastic modulus of P-LWAC. (**a**) based on number of dry-wet cycle; (**b**) based on number of silica powder content.

As demonstrated in Figure 4a, with the increase in the number of cycles, the relative dynamic elastic modulus exhibited a symmetrical trend of initially increasing and then decreasing. During the dry–wet cycle, the relative dynamic elastic modulus of all specimens was higher than 100%. The total value of the six groups of specimens reached a peak of 659.56% at 60 dry–wet cycles. Prior to the 60 cycles of salt corrosion, the pores and microcracks in the concrete initiated interactions with the salt solution. Ions in the salt solution occupy these pores and microcracks, consequently enhancing the compactness and relative dynamic elastic modulus of the concrete to an extent [67]. With the increase in the number of dry–wet cycles, the salt solution permeates the interior of the concrete and undergoes a chemical reaction with the cement, resulting in the production of corrosion products, such

as expanding sulfates. This phenomenon temporarily enhances the concrete's structure, thereby elevating the relative dynamic elastic modulus for a limited duration [66]. The relative dynamic elastic modulus reached its peak at 60 dry–wet cycles. Following 60 cycles of salt corrosion, the relative dynamic elastic modulus began to decrease. This decline is attributable to prolonged salt corrosion, leading to the deterioration of the concrete structure and manifesting in an increase in cracks and pores. Further structural damage resulted in a slight detachment of the slurry on the concrete surface, contributing to a decrease in the relative dynamic elastic modulus.

As illustrated in Figure 4b, with the increase in silica powder content, the value of the relative dynamic elastic modulus demonstrated a symmetrical trend of initially increasing and then decreasing. The relative dynamic elastic modulus of C6 reached its highest value of 110.14% after 60 dry–wet cycles. This indicates that the modest quantity of silica powder can effectively enhance the relative dynamic elastic modulus. This is due to the reaction of silica powder in the cement matrix, which produces more calcium silicate hydrates (C-S-H), improving the internal structure of the concrete [68]. As the silica powder content increased, this secondary hydration reaction became more pronounced, thereby further enhancing the stiffness and relative dynamic elastic modulus of concrete. The relative dynamic elastic modulus attained its peak at a silica powder dosage of 6%. Upon exceeding 6% silica powder content, the surplus silica powder failed to fully engage in the chemical reaction, resulting in residual unreacted particles that became sources of microscopic defects, thereby diminishing the relative dynamic elastic modulus of concrete [69].

3.3. Analysis of Compressive Strength

The compressive strength of P-LWAC following dry–wet cycles is depicted in Figure 5. It was observed that as the number of dry–wet cycles increased, the compressive strength of P-LWAC showed a symmetrical trend of initially increasing and then decreasing. Beyond 60 dry–wet cycles, compressive strength began to decline. The compressive strengths of P-LWAC with silica fume consistently surpassed those of the C-0 group, exhibiting a smoother strength change curve compared to the C-0 group. This trend is attributed to the pre-corrosion phase, where sulfate erodes the internal structure of concrete, with salt corrosion products precipitating to fill its internal pores, thereby densifying the structure and increasing compressive strength. However, as corrosion progresses, the intensified salt corrosion reaction and accumulation of salt corrosion products within the concrete's pores cause microcracks and porosity, leading to reduced compressive strength. During this phase, the microaggregate effect of silica fume renders the internal structure of P-LWAC denser, consequently mitigating the impact of sulfate on the concrete matrix [70]. Nevertheless, as the quantity of silica fumes increased, the overall compressive strength of pumice concrete exhibited a trend of first increasing and then decreasing. This is attributed to the excessive SiO_2 binding of the water in the system, thereby slowing down the cement's hydration rate and consequently initiating a decline in the concrete's compressive strength [71].

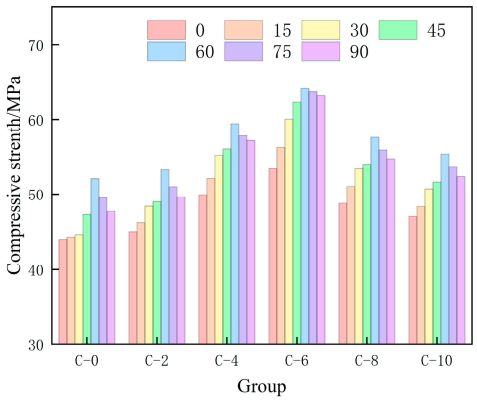

Figure 5. Compressive strength of P-LWAC after the dry–wet cycle.

Figure 6 illustrates the variation in the corrosion resistance coefficient with varying amounts of silica powder. As observed in Figure 6, with the same number of dry–wet cycles, the K value of P-LWAC with silica fumes followed a symmetrical trend of increasing and then decreasing, with the C-6 group's K value reaching 118.29%, indicating that the silica powder content at this time maximized the corrosion resistance of P-LWAC. It is worth noting that the higher K value of P-LWAC with silica fumes compared to the C-0 group is primarily attributed to the secondary hydration reaction of silica fumes, which consumes $Ca(OH)_2$ and accelerates the formation of hydrated calcium silicate (C-S-H) [72]. Additionally, the micro-aggregate effect of silica powder blocks the capillary channels in P-LWAC, enhances structural compactness, and slows down the sulfate corrosion rate. Consequently, incorporating silica powder significantly improves the sulfate corrosion resistance of P-LWAC.

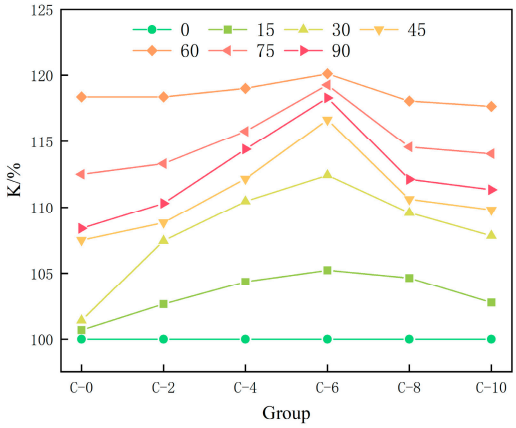

Figure 6. The relationship between the silica powder content and the corrosion resistance coefficient.

3.4. NMR Results and Analysis

3.4.1. Distribution of T_2 Spectrum

The NMR relaxation time T_2 spectrum is indicative of the pore size and distribution in P-LWAC, with the pore size being related to the peak position and the number of pores corresponding to the peak area. The larger the T_2 value, the larger the pore size. Conversely, a smaller T_2 value indicates smaller pores [73–76]. Figure 7 displays the T_2 spectral distribution for P-LWAC subjected to 0 and 90 dry–wet cycles.

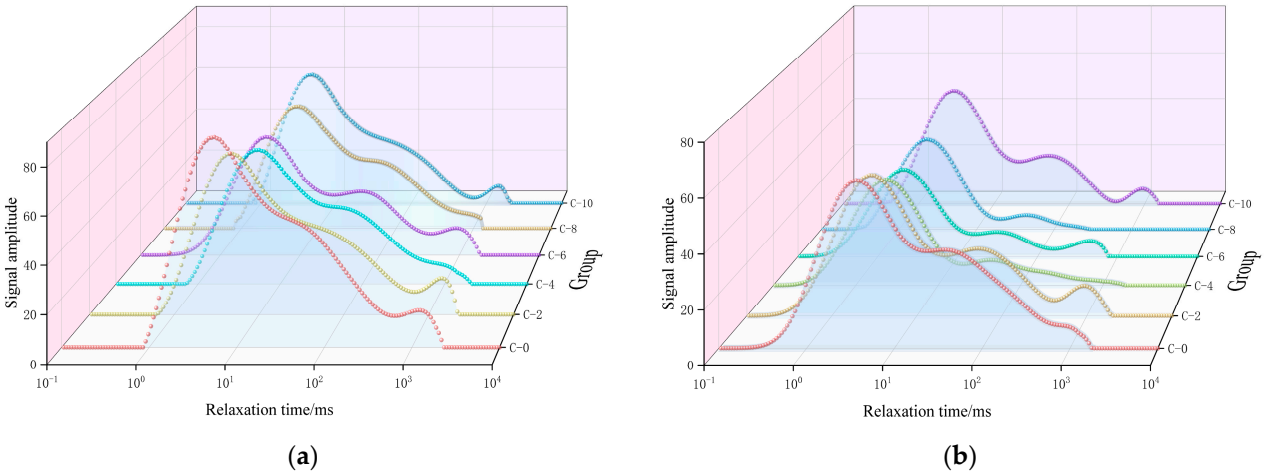

Figure 7. NMR relaxation time T_2 spectrum distribution of P-LWAC. (**a**) 0 dry–wet cycles of P-LWAC; (**b**) 90 dry–wet cycles of P-LWAC.

As depicted in Figure 7a, prior to the dry–wet cycles, compared to the C-0 group, the addition of silica powder reduced the T_2 spectral area of P-LWAC. Notably, the spectral area of standard P-LWAC was 1.2~1.6 times larger than that of the concrete mixed with silica powder. The C6 group exhibited the smallest T_2 spectral area, at a value of 3077.695. This demonstrates that the incorporation of silica powder refines the internal pore structure of P-LWAC. As observed in Figure 7b, following 90 dry–wet cycles, the addition of silica powder still reduced the T_2 spectral area. The spectral area of standard P-LWAC diminished to a value of 3584.513, remaining 1.3~2.4 times larger than that of P-LWAC mixed with silica powder. Within these results, the C-6 group exhibited the smallest T_2 spectral area at a value of 1524.938, representing a 50.5% decrease compared to the conditions before the dry–wet cycle. This indicates that the C6 group has the lowest pore size and the least number of pores at this time.

3.4.2. Distribution of Pore Size

Following the formula conversion, Figure 8 presents the pore size distribution of P-LWAC before and after the dry–wet cycles. As illustrated in Figure 8, following 90 dry–wet cycles, the maximum peak of the curve for P-LWAC was higher than the initial curve's peak, with the entire curve shifting to the left. This indicates a development towards smaller pore sizes within the structure, consequently reducing the sulfate's erosive impact on the concrete. This effect is attributed to the formation of numerous salt corrosion products during sulfate corrosion, which fill the larger pores in the concrete, leading to microcracks and an increase in smaller pores within the P-LWAC.

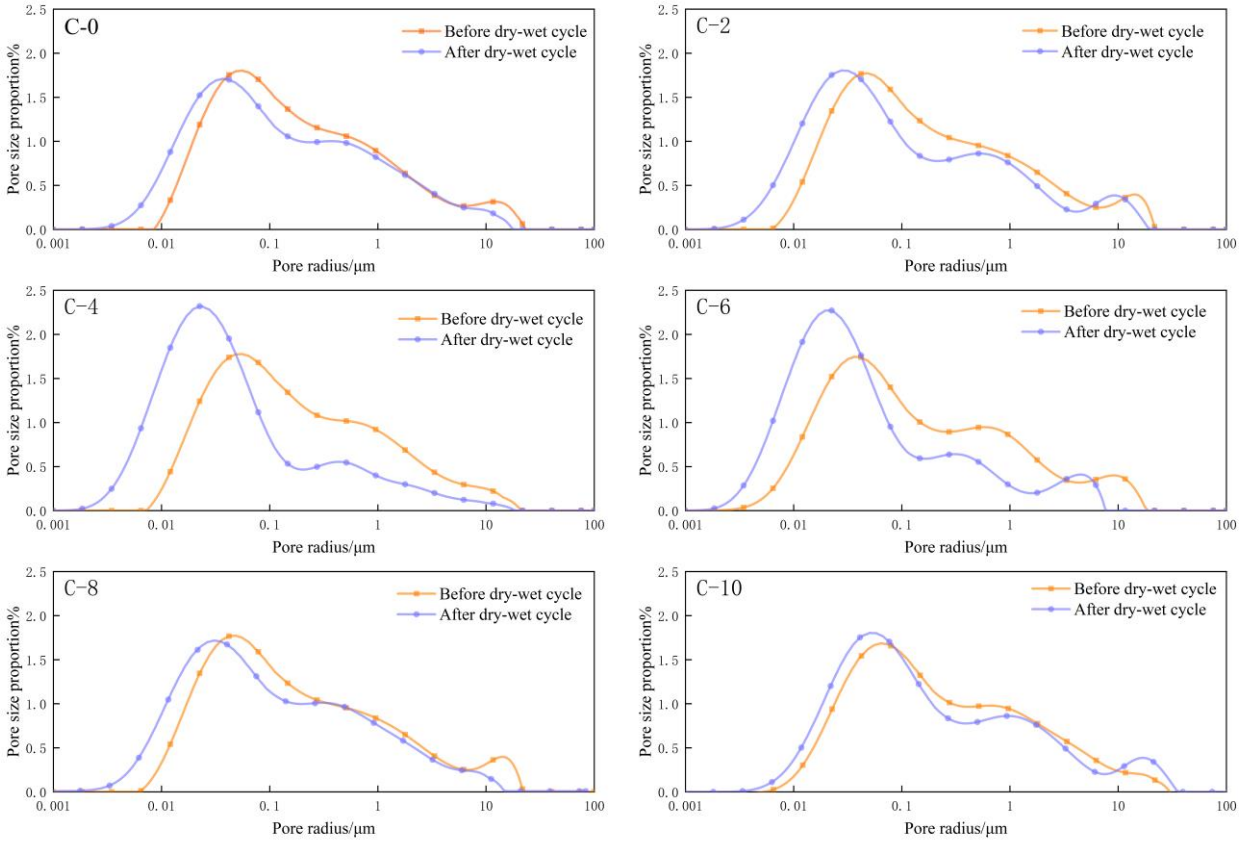

Figure 8. NMR pore radius distribution of P-LWAC.

The larger the internal pore size of concrete, the more susceptible it is to damage from corrosive substances. Therefore, concrete can be classified based on pore size: <0.02 μm for harmless pores, 0.02~0.05 μm for less harmful pores, 0.05~0.2 μm for harmful pores, and

>0.2 μm for more harmful pores [77]. Figure 9 illustrates the distribution diagram of pore radius intervals for 0 and 90 dry–wet cycles.

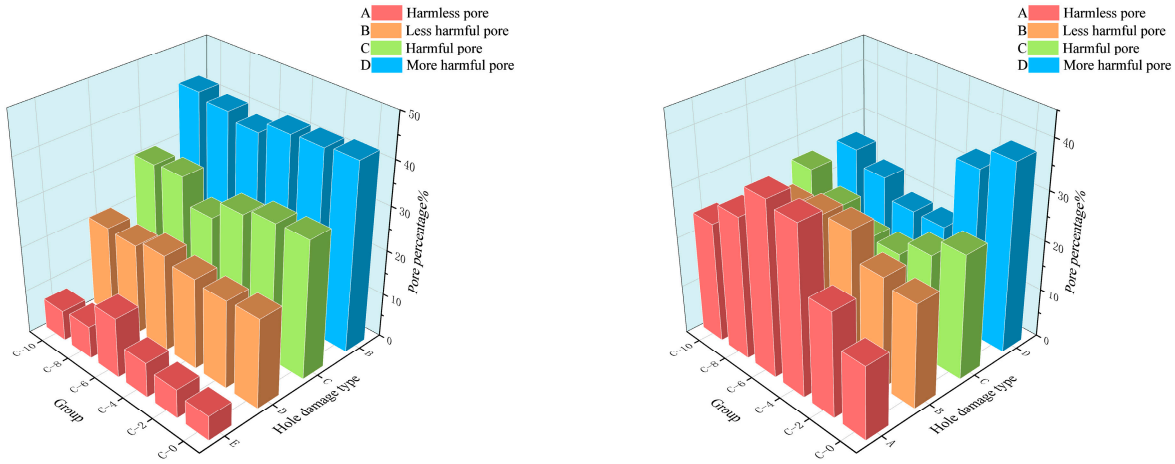

Figure 9. Pore size proportions of P-LWAC. (**a**) 0 dry–wet cycles of P-LWAC; (**b**) 90 dry–wet cycles of P-LWAC.

As observed in Figure 9, both before and after the dry–wet cycles, an increase in silica fume mixing resulted in a rise in the number of harmless and less harmful pores in P-LWAC, while the number of harmful and more harmful pores decreased. As illustrated in Figure 9a, prior to the dry–wet cycles, the C-6 group's P-LWAC showed the most significant increase in harmless and less harmful pores, rising by 38.5%, compared to the 26% increase of standard P-LWAC. From Figure 9b, it is evident that after 90 dry–wet cycles, the proportions of more harmful and harmful pores in the C-2, C-4, C-6, C-8, and C10 groups of P-LWAC were 56%, 38%, 36%, 44%, and 52%, respectively, showing symmetrical trends. These values were 11.2%, 39.7%, 42.9%, 30.2%, and 17.5% less than the 63% of standard P-LWAC, indicating a shift from more harmful and harmful pores to less harmful and harmless pores in the concrete. This change is attributed to the secondary hydration reaction between silica fume's SiO_2 and Ca $(OH)_2$, producing C-S-H that fills larger pores [78]. However, when the amount of silica fumes was higher, the relative cement content decreased, reducing the yield of C-S-H, which is not favorable for pore improvement. Thus, P-LWAC with a 6% silica powder content exhibited excellent acid corrosion resistance.

3.4.3. SEM Analysis

In order to further analyze the influence mechanism of silica powder content on the pore structure of P-LWAC, electron microscopy analysis was performed on C-0, C-6, and C-10 after 0 and 90 dry wet cycles.

As observed in Figure 10a, a small quantity of hydration products and gel substances formed on the surface of the C-0 test piece, indicating a relatively loose structure with numerous voids and the presence of lamellar crystal Ca $(OH)_2$ [79]. Figure 10b reveals that the structure of Group C-6 is notably dense, which is attributed to the secondary hydration reaction between SiO_2 and $Ca(OH)_2$ in the silica powder. The flocculent C-S-H product occupies larger pores, thereby enhancing the compactness of the P-LWAC [80]. Figure 10c illustrates that the overabundance of silica powder in the C-10 specimen leads to reduced cement content, resulting in fewer hydration products and the formation of large cracks, adversely affecting the pore structure.

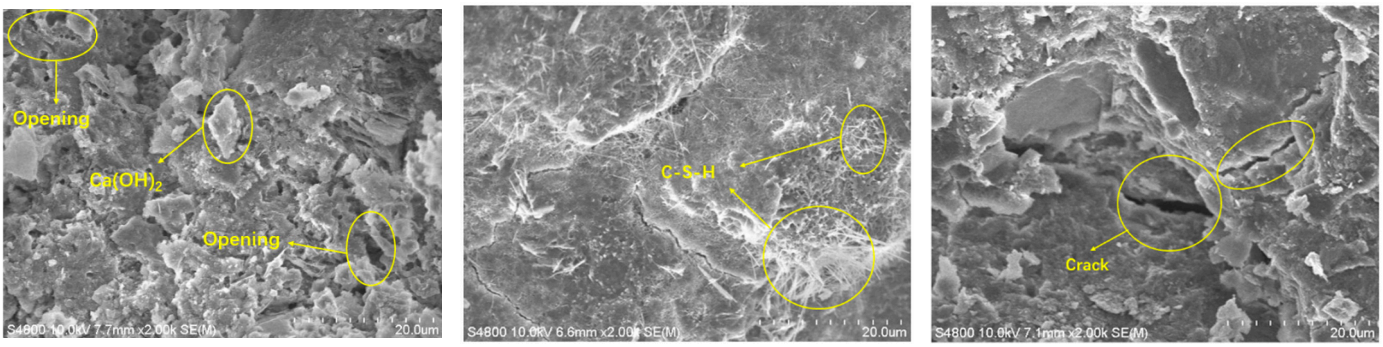

(**a**) (**b**) (**c**)

Figure 10. SEM of 0 dry–wet cycles. (**a**) C-0; (**b**) C-6; (**c**) C-10.

Figure 11a demonstrates that the number of pores on the surface of C-0 is less than before 0 dry–wet cycles. This is because after undergoing dry–wet cycles, $Ca(OH)_2$ reacts with sulfate ions to form $CaSO_4$, which fills larger pores with its density and adhesion but still has some smaller pores [81]. As indicated in Figure 11b, the structure of Group C-6 became more compact, with the flocculent C-S-H products reacting with sulfates to form calcium silicate hydrochloric sulfate hydrates, further enhancing the internal density of the P-LWAC [82]. From Figure 11c, it can be observed that C-10 formed a large amount of salt corrosion products after dry–wet cycles, filling these large cracks in the P-LWAC and resulting in the formation of small cracks and a reduction in pore size.

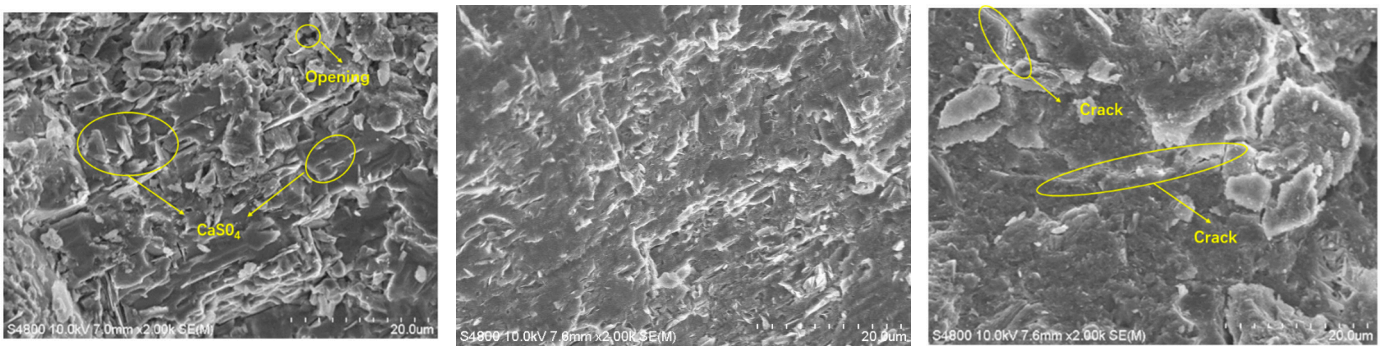

(**a**) (**b**) (**c**)

Figure 11. SEM of 90 dry–wet cycles. (**a**) C-0; (**b**) C-6; (**c**) C-10.

3.4.4. Porosity Analysis

The free water in concrete is capable of moving freely within the pores, whereas the saturation level of the bound fluid saturation is an important indicator reflecting the concrete's ability to bind liquids. This metric can reflect the internal microstructure of concrete, which includes the size and distribution of pores [83]. Therefore, this study utilized a diagram encompassing porosity, permeability, and bound fluid saturation to analyze the pore characteristics of P-LWAC, both prior to and following dry–wet cycles, as depicted in Figure 12.

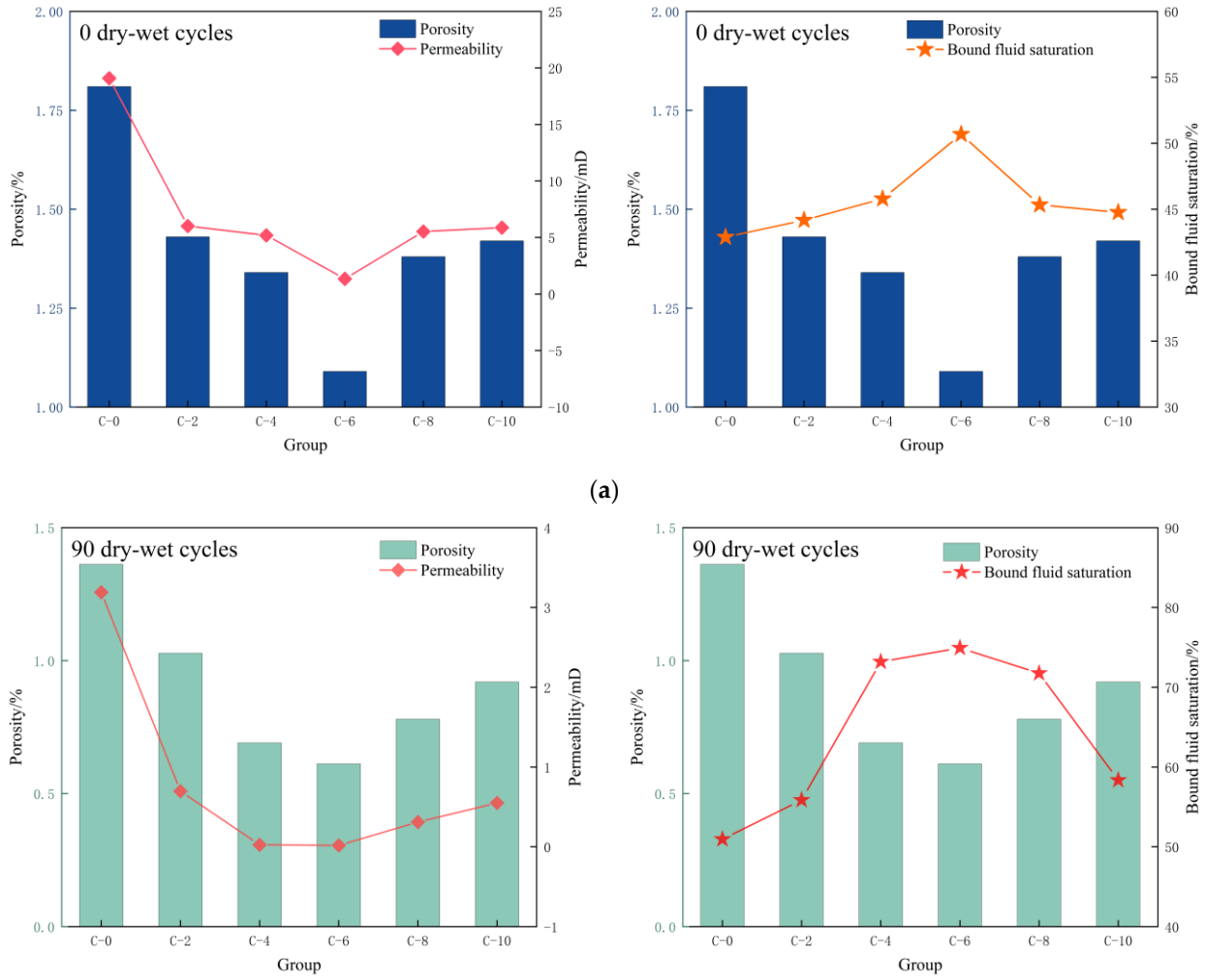

Figure 12. NMR porosity, permeability, and bound fluid saturation of P-LWAC. (**a**) 0 dry–wet cycles of P-LWAC; (**b**) 90 dry–wet cycles of P-LWAC.

From Figure 12a, it is evident that, prior to the dry–wet cycle, with the addition of silica powder, the porosity and permeability of P-LWAC diminished, while the saturation of the bound fluid escalated. In comparison to the C-0 group, the porosity exhibited reductions of 20.54%, 25.84%, 39.76%, 23.79%, and 21.59%, respectively, while the permeability displayed decreases of 68.50%, 72.77%, 92.97%, 71.02%, and 69.23%. The saturation of the bound fluid was augmented by 3.01%, 6.77%, 18.18%, 5.71%, and 4.38%, respectively. As demonstrated in Figure 12b, following 90 dry–wet cycles, the increment in silica powder content resulted in a consistent trend in the porosity, permeability, and bound fluid saturation of P-LWAC, analogous to that observed in Figure 12a. Relative to the C-0 group, the porosity underwent reductions of 24.52%, 49.27%, 55.07%, 42.73%, and 32.45%, while the permeability showed decreases of 78.15%, 99.21%, 99.44%, 90.28%, and 82.76%, respectively. The saturation of the bound fluid experienced an increase of 9.64%, 43.66%, 47.06%, 40.83%, and 14.53%, respectively. This is attributed to the fact that as the addition of silica powder, the P-LWAC structure becomes more compact, its mechanical properties are enhanced, and its permeability is diminished, thereby impeding the ingress of water into the P-LWAC's interior, leading to a reduced liquid expansion force and an augmented resistance to sulfate attack.

3.5. Established Grey Theoretical SM (1,3) Model

3.5.1. Grey Correlation Entropy Analysis of the Factors Affecting Mechanical Properties

To explore the correlation between pore characteristic parameters and the mechanical properties of P-LWAC subjected to dry–wet corrosion under varying silica powder quantities, this section examines the impact of pore characteristics of the concrete following 90 cycles. The compressive strength after 90 dry–wet cycles was chosen as the reference parameter, with spectral area, porosity, permeability, bound fluid saturation, and pore diameter intervals (<0.02 μm/%, 0.02~0.05 μm/%, 0.05~0.02 μm/%, and >0.2 μm/%) as the comparative metrics. Table 6 presents the raw data pertaining to compressive strength and pore characteristic parameters following 90 dry–wet cycles. Given that the grey entropy correlation degree assesses the significance of each factor in the overall analysis through its information entropy, it offers a more precise reflection of each factor's impact on the target variable [40]. Consequently, this study computed the grey entropy correlation degree for each attribute to accurately depict the influence of each attribute on compressive strength. The correlation between the grey entropy of compressive strength and the grey entropy of pore characteristics was calculated. The results of this analysis are displayed in Table 7.

Table 6. Raw material parameters of pore size and compressive strength of P-LWAC.

Parameter	C-0	C-2	C-4	C-6	C-8	C-10
Spectral area	3584.513	2788.335	1768.469	1524.938	1836.664	2066.746
Porosity/%	1.362	1.028	0.691	0.612	0.782	0.921
permeability/%	3.190	0.697	0.025	0.018	0.311	0.553
Bond fluid saturation/%	50.947	55.856	73.189	74.924	71.751	58.352
<0.02 μm/%	15.05	21.59	34.45	36.12	28.96	24.327
0.02~0.05 μm/%	21.32	22.7	27.84	28.16	26.66	28.89
0.05~0.2 μm/%	25.4	21.77	18.43	17.12	21.84	26.46
>0.2 μm/%	38.23	33.94	19.28	18.6	23.35	26.32
Compressive strength/MPa	47.69	49.65	57.12	63.18	54.67	52.36

Table 7. P-LWAC grey relational entropy and grey entropy correlation degree.

Parameter	Grey Relational Entropy	Grey Entropy Correlation Degree
Spectral area	1.3820	0.66458
Porosity/%	1.3813	0.66429
permeability/%	1.3313	0.64020
Bond fluid saturation/%	1.3859	0.66650
<0.02 μm/%	1.3848	0.66600
0.02~0.05 μm/%	1.3861	0.66660
0.05~0.2 μm/%	1.3840	0.66560
>0.2 μm/%	1.3849	0.66602

According to Table 7, the correlation of the compression strength was 0.02~0.05 μm/% > bound fluid saturation > greater than 0.2 μm/% > less than 0.02 μm/% > 0.05–0.2 μm/% > total spectral area > porosity > permeability. Because the larger the grey entropy correlations, the greater the influence degree, the less the correlations, the less the influence degree [84]. Consequently, the range of bound fluid saturation and the pore size category of 0.02~0.05 μm/% exerted the most significant influence on the compressive strength of P-LWAC following 90 cycles of dry–wet corrosion.

3.5.2. Grey Theoretical GM (1,3) Model Was Established

The grey model (GM) is the foundational model within grey theory, facilitating quantitative forecasts of a system's developmental trajectory [85]. Based on the calculations, the

grey theoretical GM (1,3) model identified the critical pore size range as 0.02~0.05 μm/%. Table 8 displays the raw data and 1-AGO sequences pertaining to P-LWAC.

Table 8. Raw material parameters and 1-AGO results of P-LWAC.

Parameter		Sequence	C-0	C-2	C-4	C-6	C-8	C-10
Raw material parameters	Compressive strength/MPa	x_1	47.69	49.65	57.12	63.18	54.67	52.36
	Bond fluid saturation/%	x_2	50.947	55.856	73.189	74.924	71.75	58.35
	0.02~0.05 μm/%	x_3	21.32	22.7	27.84	28.16	26.65	23.89
Dimensionless	Compressive strength/MPa	$x_1^{(0)}$	0.8813	0.9175	1.0556	1.1676	1.0103	0.9676
	Bond fluid saturation/%	$x_2^{(0)}$	0.9205	1.0091	1.3222	1.3536	1.2963	1.0542
	0.02~0.05 μm/%	$x_3^{(0)}$	0.8496	0.9045	1.1094	1.1221	1.0623	0.9521
1-AGO results	Compressive strength/MPa	$x_1^{(1)}$	0.8813	1.7989	2.8545	4.0221	5.0324	6.0000
	Bond fluid saturation/%	$x_2^{(1)}$	0.9205	1.9296	3.2519	4.6055	5.9018	6.9560
	0.02~0.05 μm/%	$x_3^{(1)}$	0.8496	1.7541	2.8635	3.9856	5.0479	6.0000

Let the GM (1,3) model be as follows:

$$\hat{x}_1^{(0)}(k) = -\mathrm{a}z_1^{(1)}(k) + b_1 x_2^{(1)} + \mathrm{b}_2 x_3^{(1)} \tag{5}$$

According to the model parameters, a is −0.4679, b_1 is −5.7039, and b_2 is 5.5941. Then, the GM (1,3) model is established:

$$\hat{x}_1^{(0)}(k) = 0.4679 z_1^{(1)}(k) - 5.7039 x_2^{(1)} + 5.5941 x_3^{(1)} \tag{6}$$

Table 9 shows the prediction results and test results of the grey theoretical GM (1,3) model. As can be seen from Table 9, the average relative error between the predicted value of the GM (1,3) model and the test value was 3.7202%, so the established model had a high accuracy and good effect. It is suitable for predicting the compressive strength of P-LWAC after dry–wet corrosion of sulfate through pore characteristic parameters.

Table 9. Comparison between experimental and predicted results of the model.

Experimental Value	Predicted Value	Residual Error	Absolute Error/%	Average Absolute Error/%
0.8813	08876	−0.0063	0.7149	
0.9175	0.9048	0.0127	1.3842	
1.0556	1.1441	−0.0885	8.3839	3.7202
1.0103	1.0339	−0.0236	2.0212	
0.9676	0.9060	0.0616	6.0972	

4. Conclusions

This study initially assessed the impact of silica powder content and the number of dry–wet cycles on the mechanical properties of P-LWAC from a macroscopic perspective. Subsequently, alterations in the internal pore structure of P-LWAC were meticulously analyzed from a microscopic perspective using NMR and SEM techniques. Ultimately, utilizing grey correlation theory, a GM (1,3) prediction model for the compressive strength of P-LWAC was developed. This model accurately predicted the durability and lifespan of concrete materials. The specific conclusions are as follows:

(1) After 60 sulfate dry–wet cycles, P-LWAC with a silica powder content of 6% demonstrated the lowest mass loss rate and the highest relative dynamic modulus, at −1.095% and 112.01%, respectively. This demonstrates that P-LWAC with a silica powder content of 6% possesses the best mechanical properties after 60 dry–wet cycles.
(2) With a constant silica powder content, the compressive strength of P-LWAC initially increased, peaking at 60 cycles before starting to decline. With increasing silica powder content, the compressive strength and corrosion resistance coefficient of P-LWAC followed a symmetrical trend of initially increasing and then decreasing. At a silica powder content of 6%, P-LWAC demonstrated the best durability.
(3) During the sulfate corrosion process, incorporating silica powder significantly reduced the pore size in P-LWAC, leading to a structural shift characterized by a transition from harmful and more harmful pores to harmless and less harmful ones. P-LWAC containing 6% silica powder featured the largest ratio of harmless pores and less harmful pores, along with the lowest porosity and permeability and the highest bound fluid saturation. These factors are pivotal in contributing to its superior durability.
(4) From the perspective of data distribution in P-LWAC with silica powder contents of 0%, 2%, 4%, 6%, 8%, and 10%, several indicators of response durability and the changing law of pore size exhibited a symmetric distribution. The symmetry center point (6%) represented the optimal silica powder content, with the performance demonstrating a mirror-like trend of variation on both sides as the content changes. This conclusion facilitates the accurate capture and understanding of the patterns of change in material performance.
(5) Following 90 dry–wet cycles, the bound fluid saturation and the aperture proportion of 0.02~0.05 μm exhibited the highest grey entropy correlation degree in P-LWAC containing silica powder. The GM (1,3) model established based on these two attributes accurately predicted the compressive strength of P-LWAC after undergoing sulfate dry–wet cycles, thereby significantly improving the efficiency of maintenance decision-making and construction of concrete materials.

5. Future Directions

This study exclusively investigated the impact of a single type of silica fume on the enhancement of concrete durability. Therefore, future research endeavors can explore the effects of silica fumes with varied particle sizes and surface characteristics on concrete performance improvements. Additionally, there is potential to examine concrete's performance under diverse environmental conditions, such as freeze–thaw cycles, chemical corrosion, high temperature and fire scenarios, ultraviolet (UV) exposure, and mechanical wear and impact.

Author Contributions: H.W. (Hailong Wang): Conceptualization, Methodology, Formal analysis, Writing—Review & Editing, Investigation; Y.C.: Writing—Original Draft, Visualization of experimental results, Formal analysis; H.W. (Hongshan Wang): Data Curation, Provision of study materials. All authors have read and agreed to the published version of the manuscript.

Funding: This research received financial backing from the National Natural Science Foundation of China, grant number 52069024, and the Major Science and Technology Special Project of Inner Mongolia Autonomous Region, grant number 2021ZD0007.

Data Availability Statement: The datasets used or analyzed in the current study are available from the corresponding author upon reasonable request.

Acknowledgments: The authors of this article greatly appreciate the assistance provided by the following personnel: Haolong Guo provided valuable suggestions on the scheme of dry–wet cycle testing, Xiong Ye helped purchase experimental materials, and Huanjie Su and Libin Shu helped maintain the testing equipment. We thank you all. The research presented in this paper was conducted with the support of Inner Mongolia Agricultural University.

Conflicts of Interest: The authors declare no conflicts of interest.

References

1. Jing, S.; Yujie, L.; Ran, Z.; Ye, L.; Yu, Z.; Qingfang, L. Experimental evaluation of fracture toughness of basalt macro fiber reinforced high performance lightweight aggregate concrete. *Constr. Build. Mater.* **2024**, *411*, 134638. [CrossRef]
2. Parung, H.; Tumpu, M.; Tjaronge, M.W.; Amiruddin, A.A.; Mansyur. Flowability and Cracks Patterns of Lightweight Concrete Subjected to Compression and Tension Loading. *Ce/Papers* **2023**, *6*, 1079–1085. [CrossRef]
3. Qing, W.; Cong, P.; Yuhang, L.; Wei, G.; Johnny, H. Pumping lightweight aggregate concrete into high-rise buildings. *J. Build. Eng.* **2023**, *80*, 108069. [CrossRef]
4. Shengwei, L.; Chengyu, B.; Jiawei, Z.; Kun, Z.; Qi, L.; Gaoming, J. Experimental study on bonding performance of GFRP bars-recycled aggregate concrete under sulfate attack environment. *Constr. Build. Mater.* **2023**, *379*, 131231. [CrossRef]
5. Gao, R.; Li, Q.; Zhao, S. Concrete Deterioration Mechanisms under Combined Sulfate Attack and Flexural Loading. *J. Mater. Civ. Eng.* **2013**, *25*, 39–44. [CrossRef]
6. Maohua, Z.; Danan, M.; Jiyin, C.; Ke, L.; Shanghui, S.; Jianfei, L. Scouring erosion resistance of nano-marine concrete under the coupled effect of chloride attack and dry-wet cycles. *Constr. Build. Mater.* **2024**, *411*, 134227. [CrossRef]
7. Jing, W.; Yangyang, X.; Chao, Z.; Chaojie, W.; Binghan, X.; Ruidong, S.; Yanhui, P.; Jianguo, C.; Pan, L.; Mingsheng, S.; et al., Evaluation of compressive strength of concrete durability degradation in dry and wet environments using destructive and non-destructive testing. *Measurement* **2023**, *223*, 113702. [CrossRef]
8. Pratap, S.R.; Raja, V.K.; Koteswaraarao, J.; Bijayananda, M. Durability assessment of fly ash, GGBS, and silica fume based geopolymer concrete with recycled aggregates against acid and sulfate attack. *J. Build. Eng.* **2024**, *82*, 108354. [CrossRef]
9. Xinxin, L.; Shouxing, W.; Fei, H.; Jinyu, Q.; Limin, L.; Qi, X.; Yongsheng, J. Mechanical relationship between compressive strength and sulfate erosion depth of basalt fiber reinforced concrete. *Constr. Build. Mater.* **2024**, *411*, 134412. [CrossRef]
10. Qian, D.; Zixiao, W.; Shaohua, L.; Qingliang, Y. Salt scaling resistance of pre-cracked ultra-high performance concrete with the coupling of salt freeze-thaw and wet-dry cycles. *Cem. Concr. Comp.* **2024**, *146*, 105396. [CrossRef]
11. Yuhao, Z.; Shiping, Y.; Luchen, W. Flexural capacity and serviceability evaluation on seawater sea-sand concrete beams reinforced by BFRP bars and TRE composite in the dry-wet environment. *Structures* **2024**, *59*, 105802. [CrossRef]
12. Xiaosa, Y.; Mingjiang, D.; Yingjie, G.; Yanbo, Z.; Fang, L. Effect on mechanical properties and microstructure of high-strength eco-friendly concrete with waste glass powder-eggshell particles. *J. Build. Eng.* **2023**, *79*, 107871. [CrossRef]
13. Zhe, X.; Yue, S.; Ziqian, H.; Yubiao, H.; Zhimin, W.; Junyu, C.; Weijian, L.; Lijuan, L.; Keting, Z.; Jiachang, K. Dynamic compression study of seawater sea sand concrete incorporated with expansive agents and glass fibre. *J. Build. Eng.* **2023**, *79*, 107942. [CrossRef]
14. Yimmy, F.S.; Silvio, D.; William, V.; Gerard, A. Performance of Self-Compacting Concrete with Residue of Masonry and Recycled Aggregate under Sulfate Attack. *J. Mater. Civ. Eng.* **2023**, *36*, 04023491. [CrossRef]
15. Qusay, A.-K.; Mohammad, A.-Q. Valorization of hydrophobic wood waste in concrete mixtures: Investigating the micro and macro relations. *Results Eng.* **2023**, *17*, 100877. [CrossRef]
16. Verma, M.; Chouksey, A.; Meena, R.K.; Singh, I. Analysis of the properties of recycled aggregates concrete with lime and metakaolin. *Mater. Res. Express* **2023**, *10*, 095508. [CrossRef]
17. Reza, F.; Amir, D.; Ashkan, S. The effect of ferrophosphorus aggregate on physical and mechanical properties of heavy-weight concrete. *Constr. Build. Mater.* **2021**, *299*, 123915. [CrossRef]
18. Samir, S.; Sattar, R.M.; Al-Mashhadi, A.S.; Basim, M.; Fadel, J.S.; Adel, M.Z.; Zainab, A.; Fatimah, A. Impact of waste materials (glass powder and silica fume) on features of high-strength concrete. *Open Eng.* **2023**, *13*, 20220479. [CrossRef]
19. Akhilesh, K.; Plaban, D. Evaluation of mechanical properties of silica fume mixed with pervious concrete pavement. *Innov. Infrastruct. Solut.* **2023**, *8*, 270. [CrossRef]
20. Khan, M.I.; Abbas, Y.M.; Fares, G. Enhancing Cementitious Concrete Durability and Mechanical Properties through Silica Fume and Micro-Quartz. *Sustainability* **2023**, *15*, 15913. [CrossRef]
21. Šoukal, F.; Bocian, L.; Novotný, R.; Dlabajová, L.; Šuleková, N.; Hajzler, J.; Koutný, O.; Drdlová, M. The Effects of Silica Fume and Superplasticizer Type on the Properties and Microstructure of Reactive Powder Concrete. *Materials* **2023**, *16*, 6670. [CrossRef] [PubMed]
22. Ahad, A.P.; Shiquan, Z.; Dengshi, H.; Feng, X.; WeiYu, L.; Qihong, Y. Application of artificial neural networks and multiple linear regression on local bond stress equation of UHPC and reinforcing steel bars. *Sci. Rep.* **2021**, *11*, 15061. [CrossRef]
23. Pishro, A.A.; Feng, X.; Ping, Y.; Dengshi, H.; Shirazinejad, R.S. Comprehensive equation of local bond stress between UHPC and reinforcing steel bars. *Constr. Build. Mater.* **2020**, *262*, 119942. [CrossRef]
24. Safdar, R.S.; Talha, A.M.; Marc, A.; Mirvat, A.B.A.; Hechmi, E.O.M.; Babeker, E.A. Effect of micro-silica on the physical, tensile, and load-deflection characteristics of micro fiber-reinforced high-performance concrete (HPC). *Case Stud. Constr. Mater.* **2022**, *17*, e01380. [CrossRef]
25. Aisheh, Y.I.A.; Atrushi, D.S.; Akeed, M.H.; Qaidi, S.; Tayeh, B.A. Influence of steel fibers and microsilica on the mechanical properties of ultra-high-performance geopolymer concrete (UHP-GPC). *Case Stud. Constr. Mater.* **2022**, *17*, e01245. [CrossRef]
26. Masoud, B.G.; Payam, A.; Reza, E.M. Enhancing mechanical performance of waste tire concrete with surface double pre-coating by resin and micro-silica. *J. Build. Eng.* **2022**, *50*, 104084. [CrossRef]
27. Suda, V.B.R.; Rao, P.S. Experimental investigation on optimum usage of Micro silica and GGBS for the strength characteristics of concrete. *Mater. Today Proc.* **2020**, *27*, 805–811. [CrossRef]

28. Ali, G.N.; Javad, N.R. The effect of nano-silica powder on mechanical and non-mechanical characteristics of self-consolidating concrete (SCC) and its impact on environment protection. *Innov. Infrastruct. Solut.* **2023**, *8*, 166. [CrossRef]
29. Yifei, Z.; Yongjun, Q.; Zheyi, G.; Dongjin, L. Research on Performance Deterioration of Multi-Walled Carbon Nanotube-Lithium Slag Concrete under the Coupling Effect of Sulfate Attack and Dry-Wet Cycles. *Materials* **2023**, *16*, 5130.
30. Liu, S.; Han, F.; Zheng, S.; Gao, S.; Zhang, G. Study on Mechanical Properties and Erosion Resistance of Self-Compacting Concrete with Different Replacement Rates of Recycled Coarse Aggregates under Dry and Wet Cycles. *Appl. Sci.* **2023**, *13*, 11101. [CrossRef]
31. Yu, F.; Zhishu, Y.; Yongjie, X.; Xinwei, L.; Xiaohu, L.; Xianwen, H. Permeability evolution and pore characteristics of reactive powder concrete of drilling shaft with initial salt erosion damage. *Constr. Build. Mater.* **2023**, *403*, 133141. [CrossRef]
32. Jianguo, L.; Wansheng, P.; Mingyi, Z.; Xusheng, W.; Jiacheng, Z.; Yindong, W. Coupled effect of the freeze-thaw cycles and salt erosion on the performance of concretes modified with nanoparticles. *Cold Reg. Sci. Technol.* **2024**, *217*, 104046. [CrossRef]
33. Ming, Z.; Shanshan, Q.; Hanxiong, L.; Chuyu, C.; Dujian, Z.; Ao, Z.; Ye, L.; Tiejun, L. A transport-chemical-physical–mechanical model for concrete subjected to external sulfate attack and drying–wetting cycles. *Eng. Fract. Mech.* **2023**, *293*, 109726. [CrossRef]
34. Jihen, M.; Othman, O.-M.; Amara, L.; Atef, D. Durability of self-compacting rubberized concrete exposed to external sulphate attack. *Case Stud. Constr. Mater.* **2024**, *20*, e02730. [CrossRef]
35. Shaojie, C.; Jianxi, R.; Xiang, R.; Yugen, L. Deterioration laws of concrete durability under the coupling action of salt erosion and drying–wetting cycles. *Front. Mater.* **2022**, *9*, 178. [CrossRef]
36. Bo, M.; Yuan, Q.; Xianwei, Z.; Jiangjiang, W.; Da, L.; Ming, L.; Heng, Z. Investigation on the change of shear strength of concrete with cold joint under the action of sulfate dry–wet cycles. *J. Build. Eng.* **2023**, *73*, 106770. [CrossRef]
37. Yating, Z.; Jiaheng, L.; Ziwei, F.; Xingyi, Z. Durability of internally cured concrete with silicon–aluminum based fine lightweight aggregate exposed to combined sulfate and wetting–drying attack. *Mater. Struct.* **2023**, *56*, 178. [CrossRef]
38. Chen, W.; Pei, F.; Zeli, L.; Ziling, X.; Tao, W.; Yingying, Z.; Yuhua, L.; Jiuhong, J. Study of the Durability Damage of Ultrahigh Toughness Fiber Concrete Based on Grayscale Prediction and the Weibull Model. *Buildings* **2022**, *12*, 746. [CrossRef]
39. Jinbao, Z.; Song, L.; Jiahui, Z. Grey Prediction Model for Drying Shrinkage of Cement Concrete Made from Recycled Coarse Aggregate Containing Superabsorbent Polymers. *Math. Probl. Eng.* **2021**, *2021*, 6662238. [CrossRef]
40. Yongli, H.; Zhengxing, Y.; Jianhua, Z.; Hongrui, Y.; Weiqing, S. Gray Model Study of Strength and Pore Structure of Recycled Concrete Powder (RCP) Concrete Based on Low-Field NMR Technology. *Materials* **2023**, *16*, 6058. [CrossRef]
41. Shuyun, Z.; Suqin, Z.; En, W.; Huijuan, D. Grey model study on strength and pore structure of self-compacting concrete with different aggregates based on NMR. *J. Build. Eng.* **2023**, *64*, 105560. [CrossRef]
42. Liu, Q.; Shen, X.; Wei, L.; Dong, R.; Xue, H. Grey Model Research Based on the Pore Structure Fractal and Strength of NMR Aeolian Sand Lightweight Aggregate Concrete. *Jom* **2020**, *72*, 536–543. [CrossRef]
43. Yin, J.; Jian, Y.; Ruoxi, D.; Xinchen, M.; Zihang, Z.; Yuxuan, Z.; Wenjie, L. Output Prediction of waste concrete based on GM (1, 1). *IOP Conf. Ser. Earth Environ. Sci.* **2020**, *525*, 012153. [CrossRef]
44. Bo, Z.; Fengfeng, Y.; Yingjie, Y.; You, W.; Cuiwei, M. Application of the novel-structured multivariable grey model with various orders to forecast the bending strength of concrete. *Chaos Soliton Fract.* **2023**, *168*, 113200. [CrossRef]
45. *JGJ55-2011*; Design Specification for Mix Proportion of Ordinary Concrete. China Concrete Industry Network: Beijing, China, 2015.
46. *50081-2002*; Standard for Test Methods for Mechanical Properties of Ordinary Concrete. Ministry of Construction of the PRC: Beijing, China, 2003.
47. *JGJ51-2002*; Technical Specifications for Lightweight Aggregate Concrete. Ministry of Construction of the PRC: Beijing, China, 2002.
48. *GB/T 50082-2009*; Standard for Testing Methods for Long-Term Performance and Durability of Ordinary Concrete. State Administration for Market Regulation: Beijing, China, 2009.
49. Luchen, W.; Shiping, Y.; Aojie, X.; Shuchun, Z. Flexural behavior of BFRP reinforced seawater sea-sand concrete beams with the TRE shell under the coupled action of dry-wet cycles and load. *Constr. Build. Mater.* **2023**, *392*, 132011. [CrossRef]
50. Zhang, M.; Cui, J.; Han, Y.; Sun, S.; Liu, K. Nitrate corrosion resistance of concrete with nanoparticles under dry–wet cycles. *Struct. Concr.* **2023**, *24*, 6709–6720. [CrossRef]
51. Maohua, Z.; Fating, X.; Yanyu, S.; Yue, H. Durability of Concrete with Nanoparticles under the Action of Both Cl− Penetration and Freeze–Thaw Cycles. *J. Cold Reg. Eng.* **2024**, *38*, 04023024. [CrossRef]
52. Hui, L.; Xinyu, L.; Xinjie, W.; Pinghua, Z.; Lei, Y.; Xiancui, Y. The impact of original aggregate and attached mortar types of recycled aggregates on the sulfuric acid resistance of geopolymer recycled concrete. *J. Build. Eng.* **2024**, *82*, 108273. [CrossRef]
53. Zhu, H.; Wen, S.; Li, X.; Li, Y.; Fu, Z. Damage Evolution of Polypropylene–Basalt Hybrid Fiber Ceramsite Concrete under Chloride Erosion and Dry–Wet Cycle. *Polymers* **2023**, *15*, 4179. [CrossRef]
54. Yonggui, W.; Meng, X.; Juan, Z. Mechanical properties and damage model of modified recycled concrete under freeze-thaw cycles. *J. Build. Eng.* **2023**, *78*, 107680. [CrossRef]
55. Wei, S.; Tiantian, G.; Pengju, H.; Xiaoyuan, W.; Fuli, M.; Bin, H. Durability study and mechanism analysis of red mud-coal metakaolin geopolymer concrete under a sulfate environment. *Constr. Build. Mater.* **2023**, *409*, 133990. [CrossRef]
56. Jing, B.; Mingxuan, S.; Yu, Z.; Chaolin, W.; Xiaojiang, D.; Kun, Z. Study on the damage characteristics of concrete-rock composite after exposure to high-temperature environments using nuclear magnetic resonance. *Bull. Eng. Geol. Environ.* **2023**, *82*, 380. [CrossRef]
57. Chen, J.; Li, Y.; Zhou, H.; Li, Y.; Guo, H. Nuclear Magnetic Resonance Study on Concrete Pore Structure Evolution Under Different Curing Environments. *Jom* **2022**, *74*, 1819–1827. [CrossRef]

58. Hebin, L.; Shouheng, J.; Xin, C.; Yong, G.; Shuhui, D. Hydration investigation of negative temperature concrete at early age based on low-field nuclear magnetic resonance. *Cold Reg. Sci. Technol.* **2022**, *194*, 103449. [CrossRef]
59. Bowen, H.; Jisheng, Q.; Peng, G.; Xujun, G.; Ruyi, Z. Freezing-Thawing Damage Mechanism of Coal Gangue Concrete Based on Low-Field Nuclear Magnetic Resonance, Scanning Electron Microscopy, and N Adsorption. *Adv. Civ. Eng.* **2021**, *2021*, 8842195. [CrossRef]
60. Shaojie, C.; Jianxi, R.; Yugen, L.; Xiang, R.; Yongjun, S.; Jielong, S. Macroscopic and Mesoscopic Deterioration Behaviors of Concrete under the Coupling Effect of Chlorine Salt Erosion and Freezing–Thawing Cycle. *Materials* **2021**, *14*, 6471. [CrossRef]
61. Lin, L.; Shuping, W.; Pengdong, Z.; Jingjing, L.; Shuang, W.; Jingxiong, Z.; Lu, Z.; Xiaofeng, Q. Effect of curing regime on the strength development and microstructure evolution of high strength concrete. *J. Build. Eng.* **2023**, *78*, 107750. [CrossRef]
62. Cheng, Y.; Sun, L.; Li, Y.; Liu, M.; He, R.; Jin, X.; Jin, H. Damage Model of Steel Fiber-Reinforced Coal Gangue Concrete under Freeze–Thaw Cycles Based on Weibull Distribution. *Materials* **2023**, *16*, 6775. [CrossRef] [PubMed]
63. Kumar, R.; Verma, M.; Dev, N. Investigation on the Effect of Seawater Condition, Sulphate Attack, Acid Attack, Freeze–Thaw Condition, and Wetting–Drying on the Geopolymer Concrete. *Iran. J. Sci. Technol. Trans. Civ. Eng.* **2021**, *46*, 2823–2853. [CrossRef]
64. Zhenbo, W.; Peng, S.; Jianping, Z.; Chang, L.; Yudong, H.; Zishan, Z. Long-term properties and microstructure change of engineered cementitious composites subjected to high sulfate coal mine water in drying-wetting cycles. *Mater. Des.* **2021**, *203*, 109610. [CrossRef]
65. Weijing, Y.; Mengyu, B.; Jianyong, P.; Tao, L. Performance degradation and damage model of rice husk ash concrete under dry-wet cycles of sulfate environment. *Environ. Sci. Pollut. Res.* **2022**, *29*, 59173–59189. [CrossRef]
66. Wei, D.; Junfeng, W. Deterioration law and life prediction of aeolian sand concrete under sulfate freeze-thaw cycles. *Constr. Build. Mater.* **2024**, *411*, 134593. [CrossRef]
67. Lv, Y.; Zhang, W.; Wu, F.; Li, H.; Zhang, Y.; Xu, G. Influence of Initial Damage Degree on the Degradation of Concrete Under Sulfate Attack and Wetting–Drying Cycles. *Int. J. Concr. Struct. Mater.* **2020**, *14*, 2988–2996. [CrossRef]
68. Jiang, J.; Li, S.; Duan, Y.; Wang, M.; Hu, J.; Hou, D.; Geng, Y.; Hu, M.; Liu, Z. Nanoscale Insights into the Protection of Calcium Silicate Hydrate by Polydimethylsiloxane Coatings in Sulfate Environments: Different Degrees of Polymerization. *Coatings* **2023**, *13*, 2004. [CrossRef]
69. Ma, G.; Liu, C.; Wu, Y.; Zheng, Z.; Liu, J.; Fang, S. The Macro and Micro Effects of Graphene Oxide and Silica Fume on the Performance of Concrete under Standard Curing Conditions. *Adv. Eng. Mater.* **2023**, *25*, 2300249. [CrossRef]
70. Azmakan, A.; Ahmadi, J.; Shahani, A.; Badarloo, B.; Garbowski, T. Optimal Quantity Investigation of Metakaolin and Silica Fume in Production of Durable Acid Resistance Alkali Activated Slag Concrete. *Buildings* **2023**, *14*, 21. [CrossRef]
71. Disheng, X.; Jinhui, T.; Xiang, H.; Yichuan, Z.; Cheng, Y.; Fangyu, H.; Jiaping, L. Influence of silica fume and thermal curing on long-term hydration, microstructure and compressive strength of ultra-high performance concrete (UHPC). *Constr. Build. Mater.* **2023**, *395*, 132370. [CrossRef]
72. Jiabin, W.; Yijie, F.; Zhihao, C.; Kaifeng, Z.; Ditao, N. Study on the durability of eco-friendly recycled aggregate concrete with supplementary cementitious materials: The combined action of compound salt solution of $MgSO_4$, Na_2SO_4, and NaCl and dry-wet cycles. *Constr. Build. Mater.* **2023**, *377*, 131149. [CrossRef]
73. Wang, J.; Dong, S.; Zhou, C.; Ashour, A.; Han, B. Investigating pore structure of nano-engineered concrete with low-field nuclear magnetic resonance. *J. Mater. Sci.* **2020**, *56*, 243–259. [CrossRef]
74. Yanlong, L.; Hui, M.; Lifeng, W.; Jianpeng, Y.; Ye, Z.; Yang, L.; Heng, Z.; Junhao, C. Influence of pore size distribution on concrete cracking with different AEA content and curing age using acoustic emission and low-field NMR. *J. Build. Eng.* **2022**, *58*, 105059. [CrossRef]
75. Lin, Y.; Zhengyuan, L.; Xie, T.; Ling, T.; Weiwei, Z. Classification of Reservoirs and Fluids in Tight Sandstone Based on the NMR Logging Technique-A Case Study of the Upper Paleozoic in the Ordos Basin. *ACS Omega* **2023**, *8*, 37882–37898. [CrossRef]
76. Arjan, K.; Sara, D.; Janez, V.; Silvana, G.; Adelaida, A. 29Si and 27Al MAS NMR assessment of the C-(A-) S–H nanomolecular structure of Ultra-High-Performance Concrete (UHPC) modified with pyrogenic oxides. *J. Indian Chem. Soc.* **2022**, *99*, 100443. [CrossRef]
77. Wu, Z.-w. High performance concrete-green concrete. *China Concr. Cem. Prod.* **2000**, *1*, 3–6.
78. Junxia, L.; Anbang, L.; Yanmeng, Y.; Xueping, W.; Fei, Y. Dry–Wet Cyclic Sulfate Attack Mechanism of High-Volume Fly Ash Self-Compacting Concrete. *Sustainability* **2022**, *14*, 13052. [CrossRef]
79. Jiang, L.; Niu, D. Study of deterioration of concrete exposed to different types of sulfate solutions under drying-wetting cycles. *Constr. Build. Mater.* **2016**, *117*, 88–98. [CrossRef]
80. Maohua, Z.; Ronghua, X.; Zenong, T.; Zhiyi, L. Durability of Marine Concrete with Nanoparticles under the Joint Effect of Dry–Wet Cycles, Cl^- Erosion, and Carbonation. *J. Mater. Civ. Eng.* **2023**, *35*, 04023464. [CrossRef]
81. Yating, Z.; Yuan, H.; Xingyi, Z. Investigation of the durability of eco-friendly concrete material incorporating artificial lightweight fine aggregate and pozzolanic minerals under dual sulfate attack. *J. Clean. Prod.* **2022**, *331*, 130022. [CrossRef]
82. Tian, W.; Libing, J.; Tai, F.; Linran, Q.; Peng, L.; Pin, Z.; Yesheng, Z. A multi-phase numerical simulation method for the changing process of expansion products on concrete under sulfate attack. *Case Stud. Constr. Mater.* **2023**, *19*, e02458. [CrossRef]
83. Menghu, Z.; Wei, D. Grey correlation analysis of macro- and micro-scale properties of aeolian sand concrete under the salt freezing effect. *Structures* **2023**, *58*, 105551. [CrossRef]

84. Yongcheng, J.; Wenwen, X.; Yichen, S.; Yulong, M.; Qiulin, H.; Zhiqiang, X. Grey Correlation Analysis of the Durability of Steel Fiber-Reinforced Concrete under Environmental Action. *Materials* **2022**, *15*, 4748.
85. Zhao, Z.F.; Chen, C.L.; Li, H.Y.; Li, L.F.; Ren, C.B. Research on influencing factors of rubber concrete performance based on grey correlation theory. *IOP Conf. Ser. Earth Environ. Sci.* **2021**, *783*, 012061. [CrossRef]